JZUS

Electronic Supplementary Materials

For https://doi.org/10.1631/jzus.A2200331

Hydrodynamics of high-speed robots driven by the combustion-enabled transient driving method

Yang YANG[2], Ying-zhong LOU[2,3], Guan-zheng LIN[2], Zhi-guo HE[1,2,4]✉, Peng-cheng JIAO[1,2,4]✉

[1] *Hainan Institute, Zhejiang University, Sanya 572000, China*
[2] *Institute of Port, Coastal and Offshore Engineering, Ocean College, Zhejiang University, Zhoushan 316021, China*
[3] *Department of Civil and Environmental Engineering, University of Washington, Seattle, WA 98195, USA*
[4] *Engineering Research Center of Oceanic Sensing Technology and Equipment of Ministry of Education, Zhejiang University, Zhoushan 316021, China*

S1 Governing equations

In this study, the finite-volume CFD software package ANSYS Fluent (ANSYS Inc., 2020) is used to simulate the Transient Driving Method of the underwater robots. The main governing equations are as follows. The Reynolds averaged model is adopted in this study. The calculation principle of the model is Reynolds's average Navier-Stokes (RANS) equations. Taking a time average and dropping the overbar on the mean velocity, the instantaneous continuity and momentum equations of the flow field around the robots can be written in Cartesian tensor form as

$$\frac{\partial \rho}{\partial t} + \frac{\partial}{\partial x_i}(\rho u_i) = 0 \tag{S1a}$$

and

$$\frac{\partial}{\partial t}(\rho u_i) + \frac{\partial}{\partial x_j}(\rho u_i u_j) = -\frac{\partial p}{\partial x_i} + \frac{\partial}{\partial x_j}\left[\mu\left(\frac{\partial u_i}{\partial x_j} + \frac{\partial u_j}{\partial x_i} - \frac{2}{3}\delta_{ij}\frac{\partial u_l}{\partial xl}\right)\right] + \frac{\partial}{\partial x_j}(-\rho\overline{u_i{}'u_j{}'}), \tag{S2a}$$

where $\overline{u_i}'$ and u_i' are the mean and fluctuating velocity components of fluid-particle in i direction respectively. ρ is the density of fluid around the robots ($998.2\text{kg}\cdot\text{m}^{-3}$ is used). p is the mean value of pressure. μ is the fluid dynamic viscosity ($\mu = 1.003\times10^{-3}$ $\text{kg}\cdot\text{m}^{-1}\cdot\text{s}^{-1}$ is used). The stress tensor due to molecular viscosity is defined by $\mu\left(\frac{\partial u_i}{\partial x_j} + \frac{\partial u_j}{\partial x_i} - \frac{2}{3}\delta_{ij}\frac{\partial u_l}{\partial xl}\right)$. The Reynolds stresses, $-\rho\overline{u_i{}'u_j{}'}$, can be related to the mean velocity gradients by employing the Boussinesq hypothesis (Alammar et al., 2014) as

$$-\rho\overline{u_i' u_j'} = \mu_t\left(\frac{\partial u_i}{\partial x_j}+\frac{\partial u_j}{\partial x_i}\right)-\frac{2}{3}(\rho k+\mu_t\frac{\partial u_k}{\partial x_k})\delta_{ij}\ , \tag{S2}$$

where μ_t is the turbulent viscosity, which can be computed as follows:

$$\mu_t = \rho C_\mu \frac{k^2}{\varepsilon}\mu_t, \tag{S3}$$

where $C_\mu = 0.09$ is a constant, k and ε are the turbulence kinetic energy and the turbulence dissipation rate in $k-\varepsilon$ model (Rahman *et al*., 2017).

This study uses standard $k-\varepsilon$ model. It's based on model transport equations for the turbulence kinetic energy (k) and turbulence dissipation rate (ε) :

$$\frac{\partial}{\partial t}(\rho k)+\frac{\partial}{\partial x_i}(\rho k u_i) = \frac{\partial}{\partial x_j}\left[\left(\mu+\frac{\mu_t}{\sigma_k}\right)\frac{\partial k}{\partial x_j}\right]+G_k+G_b+\rho\varepsilon \tag{S4a}$$

and

$$\frac{\partial}{\partial t}(\rho\varepsilon)+\frac{\partial}{\partial x_i}(\rho\varepsilon u_i) = \frac{\partial}{\partial x_j}\left[\left(\mu+\frac{\mu_t}{\sigma_\varepsilon}\right)\frac{\partial \varepsilon}{\partial x_j}\right]+C_{1\varepsilon}\frac{\varepsilon}{k}(G_k+G_{3\varepsilon}G_b)-G_{2\varepsilon}\rho\frac{\varepsilon^2}{k} \tag{S4b}$$

In these equations, G_k represents the turbulent kinetic energy generated by the mean velocity gradients, calculated as

$$G_k = -\rho\overline{u_i' u_j'}\frac{\partial u_j}{\partial x_i} = \mu_t S^2, \tag{S5}$$

while $S=\sqrt{2S_{ij}S_{ij}}$ represents the modulus of the mean rate-of-strain tensor. G_b is generation of turbulence due to buoyancy, which is given by

$$G_b = \beta g_i \frac{\mu_t}{Pr_t}\frac{\partial T}{\partial x_I}, \tag{S6}$$

where $\beta = -\frac{1}{\rho}(\frac{\partial\rho}{\partial T})_\rho$ is the coefficient of thermal expansion, g_i is the component of gravity vector in i direction and Pr_t=0.85 is the turbulent Prandtl number for energy. $C_{1\varepsilon}=1.44, G_{2\varepsilon}=1.92$ are constants respectively. $\sigma_k=1.0$ and $\sigma_\varepsilon=1.3$ are the turbulent Prandtl number for k and ε. $G_{3\varepsilon}$ determines the degree to which ε is affected by the buoyancy; it's calculated as the following relation:

$$G_{3\varepsilon} = \tanh\left|\frac{v}{u}\right|, \tag{S7}$$

where v is the velocity component parallel to the gravity vector and u is the velocity component perpendicular to the gravity vector.

S2 Numerical methods

ANSYS Fluent was used to numerically solve the governing equations. The SIMPLE scheme was used for pressure-velocity coupling. The Least Squares Cell-Based Gradient Evaluation method was used to calculate the gradients, which is much more accurate than the cell-based gradient on irregular unstructured meshes, and more efficient than the node-based gradient. The spatial discretization of the pressure equation adopted the Second Order scheme and momentum equation adopted the Second Order Upwind scheme. The First Order Upwind scheme was selected as the spatial discretization method for the turbulent kinetic energy and turbulent dissipation rate.

S3 Model validations

Here we present the validation of the developed model. The combustion-driven robot is first experimentally tested using high-speed camera (see Supplementary Video). Next, the disturbed flow field is experimentally obtained by applying the particle image velocimetry (PIV). The validation experimental setups contain two main parts that are the robot thrust setup and the PIV setup. Regarding the robot thrust setup, the robot is preset at the bottom of the flume that is filled of water. It should be noted that, to achieve the same ideal conditions as FE's, we constrained the robot so that it can only vertically move. To further simplify the validation, robots are designed with cylinder shape. Regarding the PIV setup, the laser transmitter is preset at the side of the flume to generate the X-Y profile. The tracer particles with size of 50 nm are selected.

The post-processed experimental results are shown in Fig. S1. The corresponding numerical results are shown in Fig. S2. These results present the flow fields disturbed by the thrusts of the reported robots. It can be seen that the vortices distributed at the both sides of the robots' tails are observed in Figs. S1 and S2. The high velocity regions are also observed with triangular shapes following the tails of the robots.

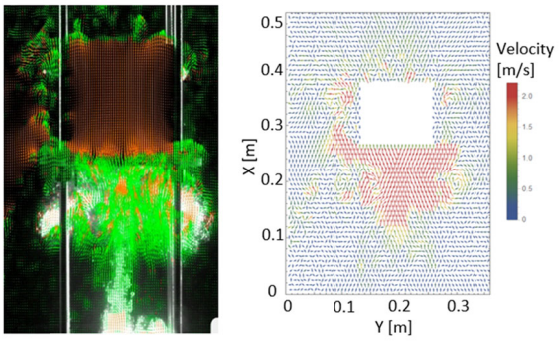

Fig. S1 Experimental results of the validation tests (t=0.1 s).

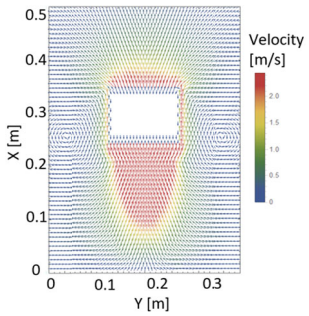

Fig. S2 The corresponding numerical results (*t*=0.1 s).

To accurately validate the model, we applied the PIV to trace fluid disturbances by the generated tiny bubbles instead of using the particles. Therefore, we applied this method to approximately validate the proposed CFD model. However, the content of the model validation is less. This is because the validation tests conducted are found with relatively low accuracy. It is challenging to conduct validation tests with high accuracy due to the following reasons:

1) The transiently high-speed motions lead to cavitation, which results in the optical refraction affecting the testing accuracy. The particle image velocimetry (PIV) is applied to conduct the validation tests. The laser is projected at the side of the robot outside the water tank. The tiny bubbles constituting the cavitation reflect the laser and are highlighted by the reflection. Therefore, it is challenging to distinguish between the highlighted particles (accurately showing the fluid field disturbance) and the highlighted tiny bubbles (NOT accurately showing the fluid field disturbance).

2) The cavitation cannot be easily eliminated experimentally and algorithmically. In the conducted validation tests, the cavitation cannot be eliminated no matter how we launch the robot. Due to the randomness of the cavitation development, it is impossible to make use of the development regulation to eliminate the cavitation by post-processing algorithms.

S4 Thrust Measurement

The measurement setup contains a base (with gas inlet and outlet holes), a soft membrane, a pushable plate with weights, and a high-speed camera. The high-speed camera starts recording the actuation process before igniting the premixed gas. Thereafter, the processes can be obtained to show the origin, explosion limit (i.e., end of the combustion) and contact limit (i.e., end of the actuation). Identifying the displacement obtained by binarizing the captured image, the velocity-time, acceleration-time, and thrust-time relations can be calculated.

S5 Drag and Added Mass Analysis

The eccentricity leads to steerings/rotations that disturb the fluid field greater to make the drag and added mass more complicated (making the overall drag greater). To prove this phenomenon from happening, a theoretical analysis of the drag and added mass with eccentricities has been developed. To determine the torque caused by the thrust force, the eccentricity factor is defined as

$$e = \frac{d}{R}, \tag{S8}$$

where d and R are the distance from the thrust force to the axial axis (i.e., the torque arm) and the radius of the robot, respectively. The added mass force F_{a} is written as

$$F_{\mathrm{a}} = \alpha F_{\mathrm{r}}, \tag{S9}$$

where α is the added mass coefficient. The drag force F_{d} is given as

$$F_{\mathrm{d}} = \frac{1}{2}\rho C_{\mathrm{d}} S_{\mathrm{p}} v^2, \tag{S10}$$

where ρ, C_{d}, S_{p} and v represent the density of water, drag coefficient, upstream area and moving velocity, respectively. S_{p} is a function of time that can be written as

$$S_{\mathrm{p}} = \frac{h(\sqrt{1+\lambda^2}-\lambda)}{2}\sin\left(2\pi t - \frac{\pi}{2}\right) + \frac{h(\sqrt{1+\lambda^2}+\lambda)}{2}, \tag{S11}$$

where h and λ are the height of the robot and ratio of the width and length of the robot, respectively. Note that α and C_{d} are affected by the geometric and motion conditions of the robot. Given the main focus of the study is to control the robot, α and C_{d} are numerically calibrated in terms of the thrust force F_{t} and e as

$$\begin{cases} \alpha_x = -21e^3 + 18.2e^2 - 0.2e \\ \alpha_y = 0.5 \end{cases}, \tag{S12}$$

where α_x and α_y are the added mass coefficient of the x and y directions, respectively. The drag coefficient is a function of the Reynolds number, which can be expressed as

$$C_{\mathrm{d}} = \frac{A}{\mathrm{Re}(t)}(1 + \varphi \mathrm{Re}(t)), \tag{S13}$$

where $A = 24$ and φ is a Reynolds adjusted parameter that is numerically fitted by simulation results as

$$\varphi = 1.375e^3 - 1.3e^2 + 0.36e + 0.1. \tag{S14}$$

References

Alammar K, 2014. Simulation of average turbulent pipe flow: a three-equation model. *Open Journal of Fluid Dynamics*, 4(1):69-73. https://doi.org/10.4236/ojfd.2014.41005

ANSYS Inc., 2020. ANSYS Ver. 18.0. https://investors.ansys.com/home/default.aspx

Rahman M, Ahmed M, Bashar M, et al., 2017. Numerical and experimental investigations on vertical axis wind turbines of different models. *Open Access Library Journal,* 4(1):1-37. https://doi.org/10.4236/oalib.1103273